Eur. J. Mineral.
2002, **14**, 331-348

Neutron total scattering method: simultaneous determination of long-range and short-range order in disordered materials

MARTIN T. DOVE[(1),*], MATTHEW G. TUCKER[(1)] and DAVID A. KEEN[(2)]

[(1)]Department of Earth Sciences, University of Cambridge, Downing Street, Cambridge, CB2 3EQ, UK
[(2)]Physics Department, Oxford University, Clarendon Laboratory, Parks Road, Oxford, OX1 3PU,
and, ISIS Facility, Rutherford Appleton Laboratory, Chilton, Didcot, Oxfordshire, OX11 0QX

Abstract: Neutron total scattering provides simultaneous information about long-range order through the Bragg peaks and short-range order through the diffuse scattering. We review recent progress in applying total scattering methods for the study of short-range structural order in silicates and other materials, focussing on changes in short-range order that accompany changes in long-range order at structural phase transitions.

Keywords: Neutron total scattering, Reverse Monte Carlo, pair distribution function, cristobalite, quartz, silica, diffuse scattering, sulphur hexafluoride.

Introduction

Powder diffraction measurements have traditionally focused on accurate measurements of the positions and intensities of Bragg peaks. The former can give a good determination of the lattice parameters, and the latter contain information about the average positions of atoms. With the development of the Rietveld method more than three decades ago, neutron powder diffraction has matured into a powerful tool for structure determination and refinement, as discussed elsewhere in this issue (Redfern, 2002). In the Rietveld method, the background scattering is modelled using polynomials with fitted coefficients. However, it is frequently found that the background contains characteristic oscillations and structure, as noted, for example, in the case of the high-temperature cubic β-phase of cristobalite, SiO_2 (Schmahl *et al*., 1992). This structured background is the diffuse scattering, which many single-crystal experiments reveal to have a strong variation across reciprocal space. Diffuse scattering contains information about fluctuations of the atomic structure from the arrangement of the average positions (see discussion in the opening paper of this issue, Dove 2002). These fluctuations contribute to the short-range structural order of the material.

The case of β-cristobalite shows clearly the type of short-range order, or fluctuations from the average structure, that can give rise to diffuse scattering. The average position of each oxygen atom lies exactly half-way between two silicon atoms (Schmahl *et al*., 1992). If this is taken literally, it implies that the Si–O–Si bond is linear, which is known to be a high-energy configuration of these atoms. Crystallographic analysis more properly gives the distribution of positions of the atoms. Usually the average position of an atom is taken to be the mid-point of its distribution of positions, and the overall distribution is often represented by a three-dimensional Gaussian function. The width of this distribution is known as the *atomic displacement parameter*. In the case of β-cristobalite, the spread of distributions of the oxygen atoms has significant elongation normal to the Si…Si vector, as shown in Fig. 1a. This implies that there is considerable bending of the O–Si–O bond, but still with the mid-point of the distribution of positions of the oxygen atoms corresponding to a linear bond. It is reasonable to ask whether the O–Si–O bond is ever linear, and whether, instead, the midpoint of the Si….Si separation is really a minimum in the distribution of oxygen positions. This would correspond to the O–Si–O bond always being bent, with the position of the oxygen atom being randomly distributed in an annulus around the midpoint of the Si…Si vector. This can be modelled in a structure refinement by using a set of equivalent positions for each oxygen atom with a partial occupancy (Schmahl *et al*., 1992). Figure 1b shows the case of refining six sites for each oxygen atom, and this leads to an improved level of agreement with the diffraction data. In crystal structure

*Author for correspondence, email: martin@esc.cam.ac.uk

0935-1221/02/0014-0331 $ 8.10
DOI: 10.1127/0935-1221/2002/0014-0331

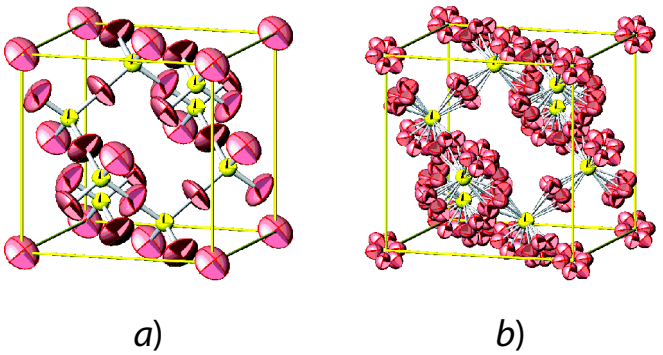

Fig. 1. The refined crystal structure of β-cristobalite, with the atoms drawn as ellipses that represent the Gaussian spread of distributions of positions (from Tucker *et al*., 2001a). In a) the distribution is shown about a single site half way along the Si…Si vector, and in b) the distribution is based on six mean sites for each oxygen atom.

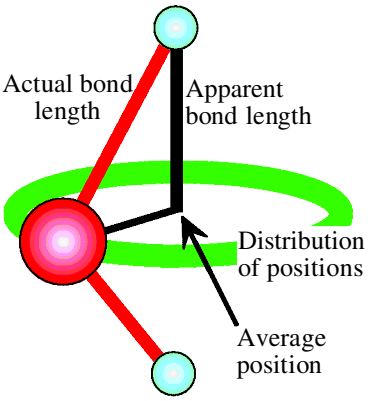

Fig. 2. The apparent shortening of the Si–O bond when the midpoint is taken to be directly between the Si…Si vector as compared to an actual position displaced from this midpoint.

analysis, the distance between mean positions is often taken to be approximately equal to the bond length. When the mean position of the oxygen atom is exactly half way between its neighbouring silicon atoms, the distance between the Si and O mean positions is significantly shorter than the normal Si–O bond length. When the mean position of the oxygen atom is taken to be one of the six sites in the annulus about the Si…Si separation, the distance between the Si and O mean positions is closer to the values of the Si–O bond length in many other tetrahedrally-coordinated silicates. This point is shown in Fig. 2.

There are, however, limits to how far one can develop this analysis. The first limitation arises from the very formalism of Bragg diffraction. Structure is properly defined by the relative positions of atoms. On the other hand, the intensities of Bragg peaks contain no information about the relative positions of atoms, only about the distributions of positions of individual atoms. Put into formal language, the relative positions of atoms are described using two particle and higher-order correlation functions, whereas Bragg diffraction is only a probe of single-atom distribution functions. The second limitation arises from the low resolution of a typical diffraction analysis. The spatial resolution of a structure is given by

$$\Delta r = \frac{2\pi}{Q_{\max}} \qquad (1).$$

$Q_{\max}$ is the largest value of the scattering vector Q used in the measurement. For scattering processes with no change in wavelength λ,

$$Q = 4\pi \sin\theta/\lambda \qquad (2).$$

In X-ray diffraction with Cu$K\alpha$ radiation (wavelength $\lambda = 1.54$ Å), the maximum value of Q is $4\pi/\lambda$, so that the resolution is $\lambda/2 = 0.77$ Å; this resolution is improved with Mo$K\alpha$ radiation, which gives minimum resolution of 0.35 Å. In a typical 6-site refinement of β-cristobalite, the distances between two closest sites in an annulus is *ca*. 0.5 Å. Clearly the 6-site model is pushing against the limits of the resolution, and at best it can only be said to be but one possible representation of the spread of positions of the oxygen atoms. Whilst it is possible to extend the range of Q, in a typical X-ray powder diffraction experiment with Cu$K\alpha$ radiation the fall-off of the atomic scattering factors with Q means that it is hard to identify Bragg peaks above the normal background before reaching $Q_{\max}$. This is not a problem with neutron diffraction, but usually for values of Q typically above 10–15 Å^{-1} there is too significant an overlap of Bragg peaks to be able to distinguish them above the background. This will give a best possible resolution of 0.4 Å in a structure refinement. It is better than with X-ray diffraction, but may still not be good enough. Furthermore, in disordered crystalline materials, there will be large atomic displacement parameters. These also will cause the Bragg peaks at higher values of Q to become too weak to be measurable, both in X-ray and neutron diffraction, and this will again limit the structural information that can be obtained from analysis of the Bragg diffraction alone.

These limitations can be effectively addressed using the method of 'total scattering'. This involves collecting the complete diffraction pattern to high values of Q, perhaps to 50–60 Å^{-1} when possible, and performing an analysis of the total diffraction pattern rather than restricting the analysis to the Bragg peaks alone. As we have noted, the total scattering will contain the diffuse scattering, and we will show below that this contains information about atomic pair distribution functions. Thus a total scattering experiment on a crystalline material is able to give simultaneous information about both the long-range crystallographic order and the short-range fluctuations. It is interesting to contrast the behaviour over both length scales in disordered crystalline materials, including some of the phases of silica, and when heating a material through a phase transition.

Total scattering methods have long been the only means of obtaining structural information on glasses or liquids (*e.g*. Wright, 1993, 1994, 1997). They are now increasingly being applied to the study of crystalline phases (*e.g*. Billinge & Thorpe, 1998), including, more recently, to the study of mineralogical materials (Dove & Keen, 1999). The first study of this type was of the α and β phases of cristobalite (Dove *et al*., 1997), and this work has been extended

to cover several other silica phases (Keen & Dove, 1999, 2000; Dove *et al.*, 2000; Tucker *et al.*, 2000a, 2001a and b). In this paper we will describe the basics of methodology, and illustrate the ideas with examples of our work on the crystalline phases of silica and on the molecular crystal SF_6.

The formalism of total scattering

We start from the equation for the interference term that defines scattering of a beam of radiation from an ensemble of atoms for a given scattering vector **Q**:

$$S(\mathbf{Q}) = \frac{1}{N}\sum_{j,k}\langle b_j b_k \exp(i\mathbf{Q}\cdot[\mathbf{r}_j - \mathbf{r}_k]) \qquad (3).$$

In a powder diffraction experiment, we need to average over all orientations of **Q** relative to the vector $\mathbf{r}_j - \mathbf{r}_k$, because we have the powder average of random grain orientations. Moreover, on instruments on time-of-flight neutron sources (such as the GEM diffractometer described below) data are collected from all around the diffraction cone and then summed. The average over all orientations of **Q** leads to the Debye result (derived, for example, in the introductory paper, Dove, 2002):

$$S(Q) = \frac{1}{N}\sum_{j,k} b_j b_k \frac{\sin(Q|\mathbf{r}_j - \mathbf{r}_k|)}{Q|\mathbf{r}_j - \mathbf{r}_k|} \qquad (4).$$

In fact the individual instantaneous atomic separations are not useful quantities, because the average is over time and hence over very many instantaneous configurations. Instead, it is better to express this function using distribution functions for the interatomic separations. We therefore need to separate the components that arise from different atoms from those that arise when $j = k$. We therefore write

$$S(Q) = i(Q) + \sum_m c_m \overline{b_m^2} \qquad (5).$$

The second term accounts for the terms in equation (4) with $j = k$, and is equal to the total scattering cross-section of the material (it is known as the *self-scattering* term). The summation is over all atom types, and c_m is the proportion of atom type m. $i(Q)$ is related to the total radial distribution function, $G(r)$, by the pair of Fourier transforms

$$i(Q) = \rho_0 \int_0^\infty 4\pi r^2 G(r) \frac{\sin Qr}{Qr}\, \mathrm{d}r \qquad (6),$$

$$G(r) = \frac{1}{(2\pi)^3\rho_0}\int_0^\infty 4\pi Q^2 i(Q) \frac{\sin Qr}{Qr}\, \mathrm{d}Q \qquad (7),$$

with average atom number density $\rho_0 = N/V$ (in atoms/Å^3). $G(r)$ may also be defined in terms of the partial radial distribution functions $g_{ij}(r)$,

$$G(r) = \sum_{m,n} c_m c_n \overline{b}_m \overline{b}_n (g_{mn}(r) - 1) \qquad (8),$$

where

$$g_{mn}(r) = \frac{n_{mn}(r)}{4\pi r^2 \rho_m \mathrm{d}r} \qquad (9).$$

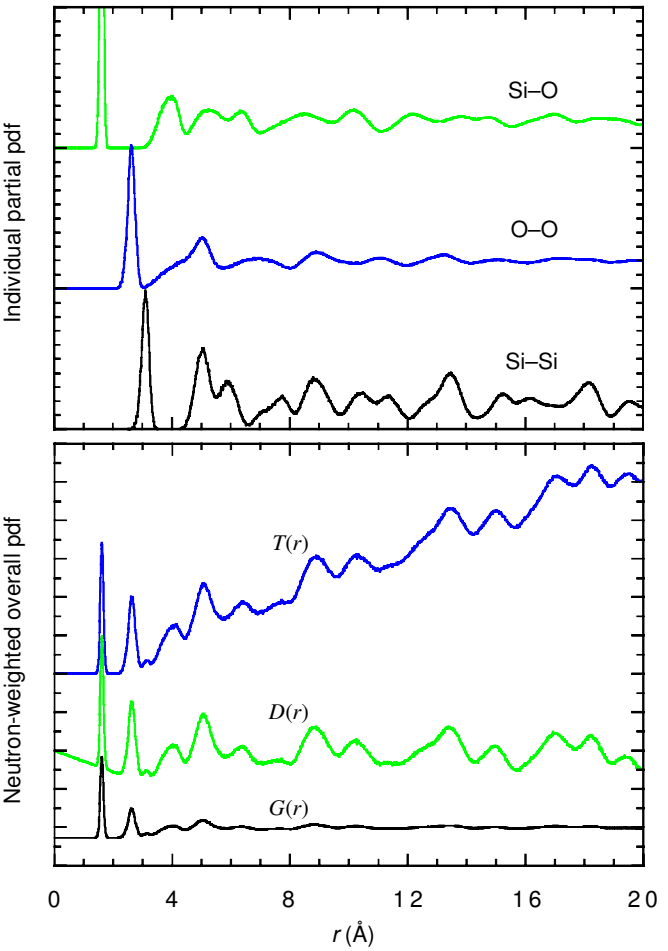

Fig. 3. Example of the representation of the pair distribution functions (pdf) obtained for β-cristobalite at 300°C. *Top* shows the Si–O, Si–Si and O–O partial pdf functions (origin displaced), each of which tend to values of unity at large r by definition. *Bottom* shows the merging of the three partial distribution functions into the neutron-weighted overall functions. $G(r)$ is the weighted sum of the partial pdf functions (equation 8), which tends to the value $\sum_{m,n} c_m c_n \overline{b}_m \overline{b}_n$ at $r = 0$, and to a value of zero at large r. $D(r)$, obtained from $G(r)$ *via* equation (10), oscillates around zero for large distances, and approaches zero linearly from negative values as r tends to zero. $T(r)$, obtained from $D(r)$ *via* equation (13), has zero value at low r, and oscillates around a line of constant slope at larger values of r. $D(r)$ shows the structure in the pair distribution function most clearly at intermediate and large values of r, whereas $T(r)$ shows most clearly the pair distribution functions for the nearests-neighbour bonds.

$n_{mn}(r)$ is the number of particles of type n between distances r and $r + \mathrm{d}r$ from a particle of type m and $\rho_m = c_m\rho_0$. Two other versions of correlation functions are commonly used. *First*, the differential correlation function, $D(r)$, is defined as

$$D(r) = 4\pi r \rho_0 G(r) \qquad (10).$$

Thus we can write equations (6) and (7) as

$$Qi(Q) = \int_0^\infty D(r) \sin Qr \, dr \quad (11),$$

$$D(r) = \frac{2}{\pi} \int_0^\infty Qi(Q) \sin Qr \, dQ \quad (12).$$

Second, the total correlation function, $T(r)$, is defined as

$$T(r) = D(r) + 4\pi r \rho_0 \left(\sum_m c_m \bar{b}_m \right)^2 \quad (13).$$

These different functions are illustrated schematically in Fig. 3. Technically, the function $rG(r)$ is the transform of the experimentally derived quantity $Qi(Q)$, and thus best reflects the direct analysis of experimental data. $T(r)$ is useful because it has a value of zero below the first few peaks, and $D(r)$ is useful because at larger distances it oscillates around zero.

A number of alternative representations of the nomenclature of total scattering are in common use. Keen (2001) has compared several of these – we follow closely the recommendations given in that paper. The formalism is also reviewed by Wright (1993, 1994, 1997).

Experimental methods

Basic requirements

Neither the experimental procedure necessary for performing total scattering measurements, nor the treatment of data prior to detailed analysis, are trivial. There are three main experimental constraints. The *first* of these is that it is necessary to perform measurements to relatively large values of Q, following the earlier discussion concerning the fact that the resolution is given by the inverse of Q_{max}. For an experiment performed with Cu$K\alpha$ X-radiation and collecting data to $2\theta = 180°$, the resolution is around half of the length of a Si–O bond. Ideally it would be useful to aim for a resolution that is a small percentage of a bond length. With time-of-flight neutrons, it is possible to obtain good data to values of Q of around 60 Å^{-1}, and even higher if necessary (albeit with the caveat that the data quality is lower at higher values of Q and therefore more experimental effort would be required). This will give a resolution of around 0.1 Å, which is *ca.* 6% of the Si–O bond length.

The *second* essential experimental condition arises from the fact that the total scattering needs to be a good integration over all possible changes in energy. The neutrons can be scattered *elastically* with no change in energy (as in Bragg scattering), or scattering *inelastically* with either a gain in energy due to the absorption of one or more phonons or a loss in energy due to creation of one or more phonons. For an accurate total scattering experiment, all these processes must be allowed to occur. The last condition is the hardest. It implies that the energy of the incident neutron beam must be higher than the energy scale of the phonons in the material.

The *third* experimental requirement is that *background* scattering (*i.e.* scattering from sources other than from the sample) needs to be minimised, and that it must be possible to measure to high values of Q with good statistical accuracy. Variations in $S(Q)$ are much weaker at higher values of Q, which means that data at these values need to be good if the ripples are to be used to provide information about structure over short distances.

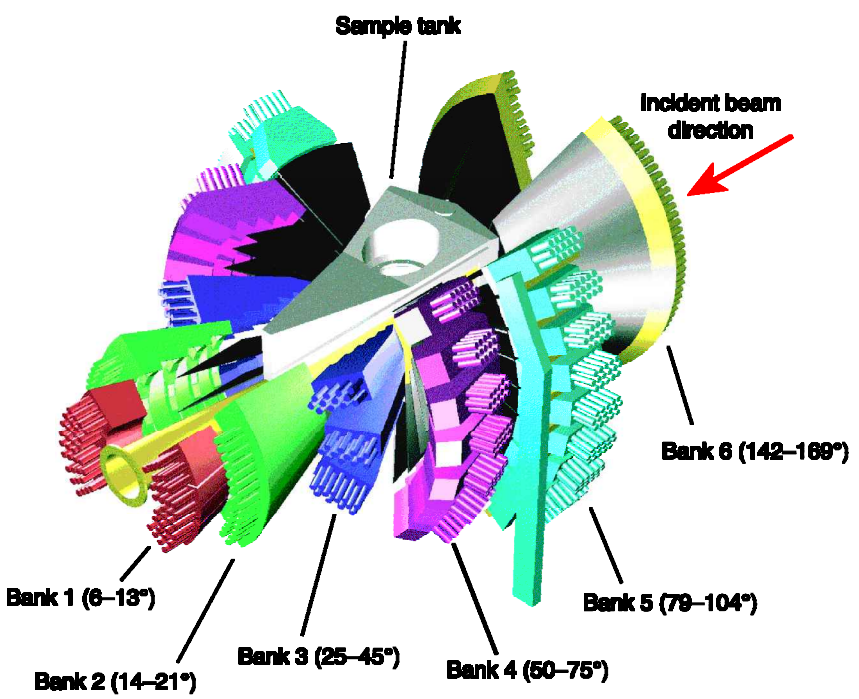

Fig. 4. Schematic diagram of the GEM diffractometer at ISIS (Williams *et al.*, 1998), showing the banks of detectors that cover most of the scattering angles. This instrument has been optimised for both pure diffraction (high resolution and high intensity) and total scattering (detectors covering a wide range of Q with high intensity and high stability). The higher angle banks have the higher resolution in Q and allow measurements to higher values of Q, whereas the lower-angle banks allow measurements to low values of Q.

As a result of these three requirements, the best data are obtained at spallation time-of-flight neutron sources. There is a rich flux of high-energy neutrons, and with appropriate instrument design there are no geometric constraints on the range of Q accessible for measurements. Certainly it is quite possible to obtain good data for values of Q in excess of 60 Å^{-1}, beyond which it is often found that the total scattering signal has reached a constant value (*i.e.*, $i(Q) = 0$). The instrument GEM at ISIS is ideal for total scattering experiments, giving large values of Q_{max}, low intrinsic background, and high resolution for measurement of Bragg peaks, in addition to having a high coverage of the range of scattering angles with banks of detectors. This instrument is shown in Fig. 4. A reactor source of neutrons has its largest distribution of neutron energies at lower energies, so that data can typically be obtained to Q_{max} ~ 20 Å^{-1}. Synchrotron sources can also produce high-energy beams of X-rays to permit measurements to Q_{max} ~ 30–40 Å^{-1}; we expect to see an increasing use of synchrotron X-ray beams for total scattering measurements.

Basic data reduction

The formalism and interpretation of total scattering experiments are both firmly grounded in the possibility of the measurements giving absolute values of the intensity of the scattered beam. This is quite different from some other neutron scattering techniques. For example, in the Rietveld method, the scale factor is treated as an adjustable parameter, a number of adjustable parameters are used to define a background function (which is often treated as a polynomial), and other factors such as absorption and extinction coefficients can also be treated using adjustable parameters. The values of all these parameters can be varied in the least squares refinements, and finally should have little effect on the quantitative values of the important refined structural parameters. On the other hand, there is no scope for the use of adjustable parameters in the analysis of total scattering. The scale factors, background, and absorption corrections need to be known absolutely. This means that all corrections need to be measured separately, or it must be possible to calculate them. The set of corrections (discussed in Howe *et al*., 1989; Wright, 1993, 1994, 1997) is:

1 One set of corrections accounts for background scattering from the components of the instrument, the equipment used to control the sample environment (furnaces or cryostats), and the sample container. These three experimental components, together with the sample, also give an attenuation of the signal, which needs to be accounted for. The procedure for performing these corrections is outlined in the appendix.
2 The data also need to be properly normalised. Account needs to be taken of multiple scattering (*i.e.*, processes in which the beam is scattered more than once within the sample), and of factors such as the energy spectrum of the incident beam, solid angles of the detectors, and detector efficiencies. Multiple scattering can be calculated for a sample that does not scatter an appreciable fraction of the incident beam (typically up to around 20%). Its contribution tends to be constant with Q.
3 The energy spectrum of the incident beam is easily measured using a special detector, called the monitor, positioned just in front of the instrument. All measured spectra must be scaled by the spectrum recorded in the monitor. The factors concerned with the detectors can be taken into account by performing a measurement of the incoherent scattering from a sample of vanadium that is ideally of the same size as the sample. The coherent Bragg scattering from vanadium is extremely weak (which is why it is so useful in this context). However, the Bragg peaks can still be observed in the measurement, and are taken account of by fitting the vanadium scattering with a smooth function that lies below the Bragg peaks. The intensity of the incoherent scattering from vanadium is known theoretically (it is independent of Q and given by the inelastic cross section), and therefore the normalisation of the measurements is straightforward. Multiple scattering corrections need to be applied also to the scattering from the vanadium used for normalisation.
4 The other important correction is known as the *Placzek correction*. In an X-ray experiment, the changes in energy of the scattered X-ray beams are tiny compared to the energy of the incident beam. This means that the scattered beam has almost the same wavelength as the incident beam, and when scattering at a fixed angle the value of Q can be established from the equation (2). However, in neutron scattering, the change in energy gives rise to a significant change in wavelength. In a total scattering experiment, there is no measurement of the energy of the neutrons when they reach the detectors, and hence the wavelength is unknown. In effect, the integration over energy implicit in a total scattering experiment is performed at constant scattering angle rather than constant Q. The correction required to bring the integral back to constant Q is the *Placzek* or *inelasticity correction*. It also needs to account for the fact that the efficiency of a detector typically scales as the inverse of the neutron velocity. The Placzek correction can be calculated for simple atomic systems (see, for example, Bacon, 1975; Chieux, 1978), and these corrections can be adapted for more complex systems or for different experimental arrangements.

Data reduction and analysis of $G(r)$

Once the data have been corrected as outlined above, the task is to obtain $G(r)$ or its alternative forms. With the data properly normalised, the first stage is to subtract the self-scattering term from $S(Q)$ to give $i(Q)$ (equation 5), and then to generate $Qi(Q)$ for the Fourier transform of equation (12). The functions $i(Q)$ and $Qi(Q)$ are compared in Fig. 5, showing the range of detail within the data, including the oscillations in $Qi(Q)$ at large Q that reflect the structure of polyhedral units within the material.

If data are collected in a single measuring process, such as from one set of detectors, a single function $Qi(Q)$ can be constructed for Fourier transform. There are two issues that need to be considered. The *first* is that the Fourier trans-

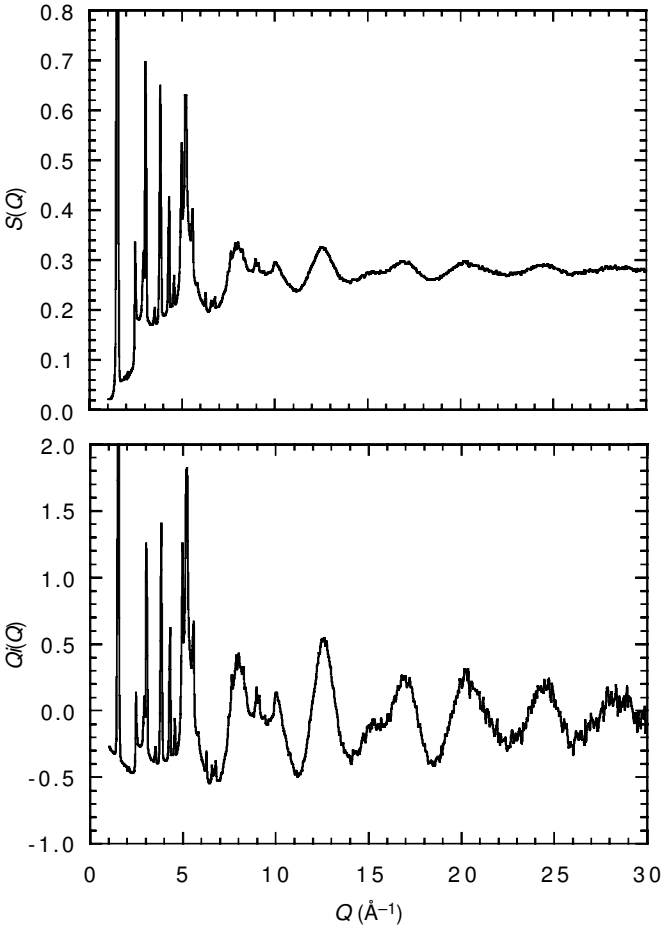

Fig. 5. Representation of the $S(Q)$ and $Qi(Q)$ functions obtained for β-cristobalite at 300°C, where $i(Q)$ is simply obtained from $S(Q)$ by sutracting the constant value to which $S(Q)$ tends at large Q (Tucker *et al.*, 2001a). The $Qi(Q)$ function highlights the oscillations out to large values of Q.

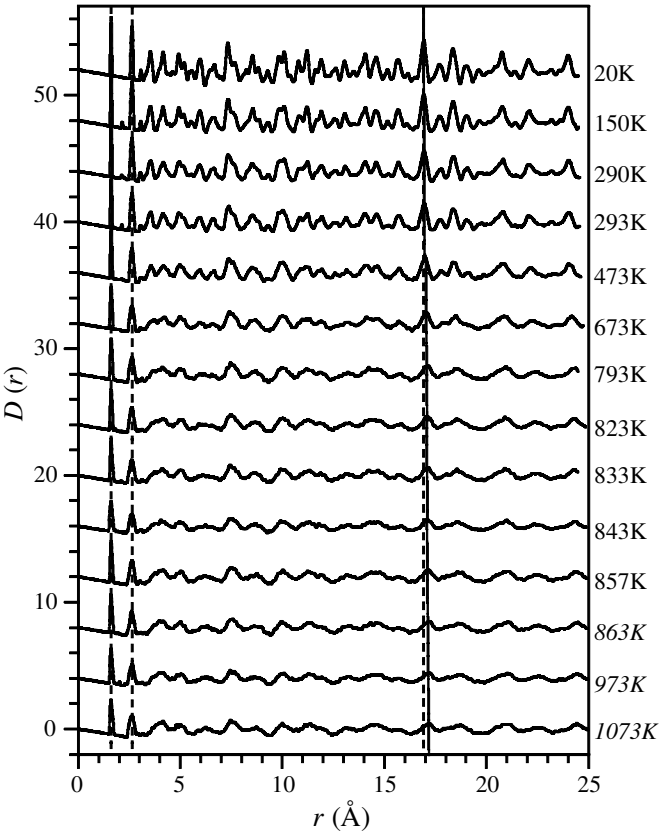

Fig. 6. $D(r)$ functions for quartz across a wide range of temperatures, showing progressive broadening of the main features as temperature is increased. The left-hand near-vertical dashed line shows the small variation of the Si–O peak with temperature. The right-hand near-vertical solid line shows how the cube root of the crystal volume varies with temperature, highlighting how the main structural features at intermediate distances scale with the thermal expansion of the crystal by comparison with the right-hand dashed line that is exactly vertical.

form will contain 'truncation ripples' due to the finite range of Q being used. These are reduced if Q_{max} is increased, particularly if $Qi(Q)$ is close to zero at Q_{max}. It is common to multiply $Qi(Q)$ by a modification function $M(Q)$ that falls smoothly to zero at Q_{max}, such as

$$M(Q) = \frac{\sin(\pi Q/Q_{max})}{\pi Q/Q_{max}} \qquad (14)$$

(Wright, 1994). Whilst this reduces the termination ripples in the Fourier transform, it does mean that the resultant $G(r)$ is convoluted with the Fourier transform of $M(Q)$. This leads to a broadening of the peaks in $G(r)$, which is particularly significant for low values of Q_{max}.

The *second* issue in the analysis of $i(Q)$ is that the measurements will contain the effects of the experimental resolution. If the resolution is not taken into account, its effect will be that the resultant $G(r)$ will be multiplied by the Fourier transform of the resolution function. This will lead to a reduction in the size of $G(r)$ on increasing r. The issue of resolution is not trivial, since the resolution function is actually a function of Q.

On instruments such as GEM (Fig. 4), different sets of detectors will measure $i(Q)$ for different ranges of Q, and the data will need to be combined in some way to perform the Fourier transform of equation (12). One approach might be to paste the measurements of $i(Q)$ for different ranges of Q into one single overall $i(Q)$ function. However, each set of detectors will be subject to a different resolution function, and it is not possible to properly account for this in the subsequent Fourier transform. One solution to the problem is to construct $G(r)$ using inverse Fourier methods. In this approach, a trial form of $G(r)$ is adjusted until its Fourier transform is in close agreement with the experimental measurements of $i(Q)$. It is relatively straightforward to account for resolution in this approach, and there are no termination ripples. The inverse Fourier transform can be compared with any number of sets of data, each with different ranges of Q and resolution. We use a Monte Carlo method to adjust the trial form of $G(r)$ pointwise, using the MCGR program of Pusztai & McGreevy (1997) modified to account for the resolution from time-of-flight neutron

instruments. This modified program is called MCGRtof, and is described in detail elsewhere (Tucker *et al*., 2002a).

The analysis of $G(r)$ or its alternative representations can be considered with two aspects. The *first* is the analysis of the distinct peaks at low r. These contain information about the true distribution of interatomic distances, which may be different from the distances between the mean positions determined by crystal structure refinement from the intensities of the Bragg peaks. This is illustrated by our measurements on quartz (Tucker *et al*., 2000a, 2001b). The $D(r)$ functions over a wide range of temperatures, encompassing the α–β displacive phase transition, are shown in Fig. 6. The position of the first peak gives the mean instantaneous Si–O distance, which is denoted as $d_{\langle Si–O\rangle}$ and shown as a function of temperature in Fig. 7. This is compared with the temperature-dependence of the distance between the mean positions as obtained from analysis of the Bragg peaks, denoted as $d_{\langle Si\rangle–\langle O\rangle}$. These distances were obtained by Rietveld refinement of the same data used to obtain $G(r)$. Clearly the temperature dependence of $d_{\langle Si–O\rangle}$ is different from that of $d_{\langle Si\rangle–\langle O\rangle}$, with the former showing only a weak positive variation with temperature and the latter having a significant variation that reflects the phase transition. In particular, $d_{\langle Si\rangle–\langle O\rangle}$ decreases on heating, particularly on heating in the high-temperature β-phase, and it is probable that this can be understood as a result of increased rotational vibrations of the SiO_4 tetrahedra which give the appearance of bond shortening. This difference between $d_{\langle Si–O\rangle}$ and $d_{\langle Si\rangle–\langle O\rangle}$ is even more acute in β-cristobalite if the average position of the oxygen atom is taken to be half way between two silicon atoms (Tucker *et al*., 2001a). Even when using the split-site model, the distance between the mean postions of the silicon and oxygen atoms is still lower than the mean instantaneous Si–O distance.

The analysis of the pair distribution functions has been carried out on a number of silica phases. The overall temperature dependence of the Si–O bonds in all phases is shown in Fig. 8 (Tucker *et al*., 2000b). From the analysis we obtained a value for the coefficient of thermal expansion of the Si–O bond of 2.2 (± 0.4) × 10^{-6} K^{-1}. Other attempts to determine the intrinsic temperature dependence of the bond have been indirect, through applying corrections to the crystal structure from detailed analysis of the thermal displacements parameters (Downs *et al*., 1992). The coefficient of thermal expansion obtained from $G(r)$ is lower than that obtained by indirect analysis from the crystal structure (see discussion of Tucker *et al*., 2000b).

The *second* aspect of the analysis of $G(r)$ concerns its form for distances beyond the first few peaks. There will be too many overlapping peaks to be able to identify specific neighbour distances, but this region of $G(r)$ can provide information about mid-range order. Consider the $D(r)$ functions for quartz shown in Fig. 6. The main features across all distances broaden on heating, which shows the increase in thermal disorder. Many features vary smoothly though the α–β phase transition without significant change. In particular, the positions of the lower-r peaks vary only slightly with temperature. However, the positions of some of the features at larger r have a variation with temperature that reflects the variation of the volume of the unit cell, which in turn has a variation with temperature that is strongly correlated with the displacive phase transition. The case of cristobalite is particularly interesting for the mid-range distances (Dove *et al*., 1997; Tucker *et al*., 2001a). For distances greater than 5 Å, the features in $G(r)$ are quite different, which can be traced to changes in the oxygen–oxygen partial distribution functions (Tucker *et al*., 2001a). This shows that the structure of β-cristobalite is

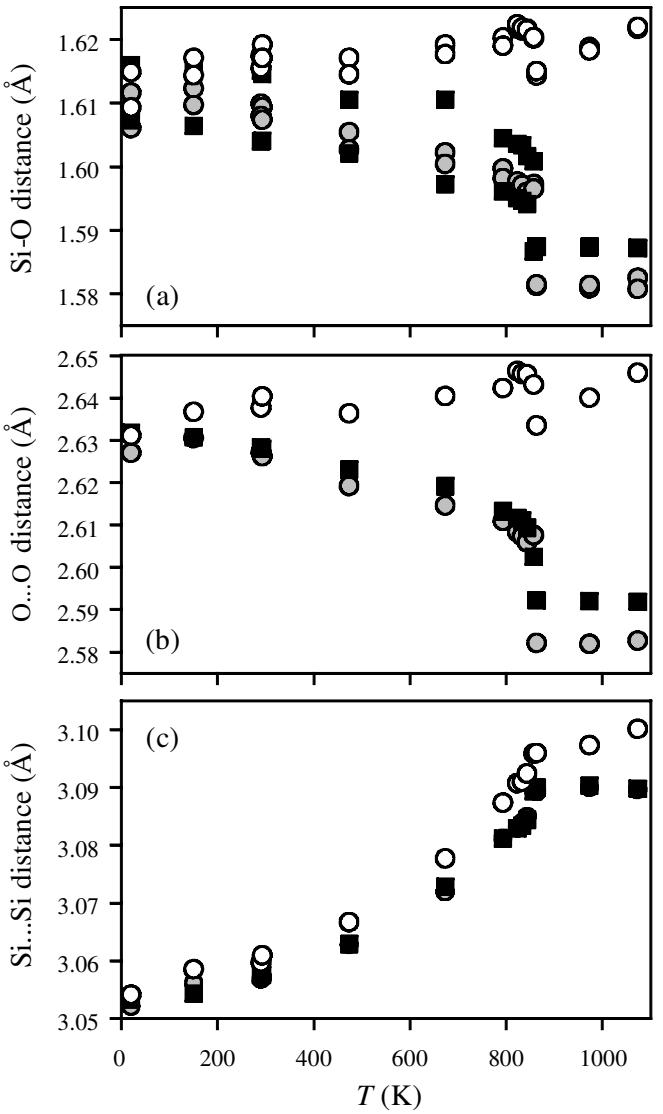

Fig. 7. Comparison of the temperature dependence of the average instantaneous Si–O, O–O and Si–Si shortest interatomic distances in quartz obtained from the pair distribution functions (open circles), and compared with the distances between the mean positions obtained from crystal structure refinements (filled squares) and the RMC analysis (filled circles). The crystal structure has two distinct distances between the Si and O distances, which are shown separately. The instantaneous Si–O and O–O distances vary only weakly with temperature, whereas the distances between the mean positions are clearly affected by the α–β displacive phase transition. The variations of both the instantaneous Si–Si distance and the distance between the mean positions of neighbouring Si atoms reflect the phase transition on heating.

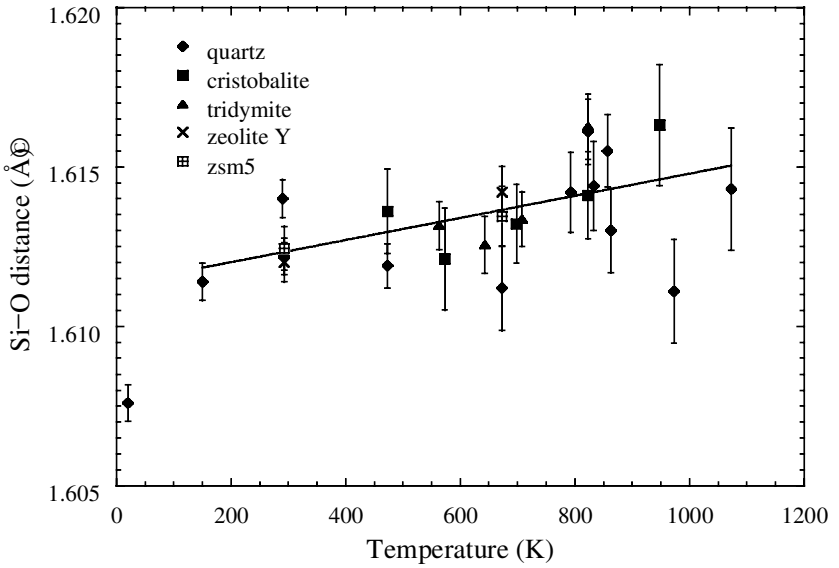

Fig. 8. Overall thermal expansion of the Si–O bond for a range of silica polymorphs, obtained from the corresponding peak in the pair distribution function obtained by neutron total scattering (Tucker *et al*., 2000b).

significantly different from that of α-cristobalite over distances as small as one unit cell length. A similar analysis has been carried out for the high-temperature phase of tridymite (Dove *et al*., 2000).

Reverse Monte Carlo modelling

The obvious question posed by the preceding discussion is how the crystal structure of a material such as quartz or cristobalite can accommodate a significant difference between the instantaneous Si–O bond length and the distance between the mean positions of the two atoms. The fact that there have been various proposals in the literature for the structures of the high-temperature disordered phases in the cases of quartz and cristobalite (and also to a lesser extent in tridymite, where the issues are similar) suggests that this issue is not trivial. What is required is a data-based model for the whole structure that goes beyond consideration only of nearest-neighbour distances. The Reverse Monte Carlo (RMC) method (McGreevy & Pusztai, 1988; McGreevy, 1995) provides one useful tool in this direction.

The basis of the RMC method is straightforward. The atomic coordinates in a configuration are adjusted using a Monte Carlo algorithm to improve agreement between calculated functions and experimental data. For total scattering measurements, the important data are $G(r)$ or $i(Q)$ (or their variants). An energy function can be defined with the following form based on the differences between the calculated (subscript 'calc') and experimental (subscript 'exp') values of $i(Q)$ and $G(r)$:

$$\begin{aligned}
\chi^2_{\mathrm{RMC}} &= \sum_m \chi^2_m \\
\chi^2_{i(Q)} &= \sum_k \sum_j \left[i_{\mathrm{calc}}(Q_j)_k - i_{\mathrm{exp}}(Q_j)_k \right]^2 / \sigma^2_k(Q_j) \\
\chi^2_{G(r)} &= \sum_j \left[G_{\mathrm{calc}}(r_j) - G_{\mathrm{exp}}(r_j) \right]^2 / \sigma^2(r_j) \\
\chi^2_f &= \sum_\ell \left[f_\ell^{\mathrm{calc}} - f_\ell^{\mathrm{req}} \right]^2 / \sigma^2_\ell
\end{aligned} \qquad (15).$$

The σ variables give specific weightings, and can be related to experimental standard deviations, or set to favour one type of data over another. The last term in equation (15) matches any quantity calculated in the RMC configuration, which we denote as f^{calc}, against a pre-determined (or required) value f^{req}, and acts as a set of constraints. The most common form of constraint is on bond lengths or bond angles (Keen, 1997, 1998). These constraints need not be artificial, and can be based on the same experimental data. For example, if a bond length constraint is used, the value of the bond length can be set to equal the position of the corresponding peak in $G(r)$, and the spread of bond lengths as controlled by the value of σ^2 can be equated to the width of the corresponding peak in $G(r)$.

The starting point is a configuration of atoms based on a model structure, which will be the average crystal structure when the analysis is being carried out on crystalline materials. The Monte Carlo process involves a series of steps in which an atom is chosen at random and then moved by a random amount. This will lead to a change in the value of χ^2_{RMC}, which we denote as $\Delta\chi^2_{\mathrm{RMC}}$. If $\Delta\chi^2_{\mathrm{RMC}}$ is negative, the change is accepted and the process repeated. If $\Delta\chi^2_{\mathrm{RMC}}$ is positive, the move is accepted with probability $\exp(-\Delta\chi^2_{\mathrm{RMC}}/2)$. The process is repeated for many steps, until χ^2_{RMC} oscillates around a stable mean value.

The RMC method was developed by McGreevy & Pusztai (1988), initially to use total scattering data for the development of structural models of fluids and glasses for which there is no equivalent of an average crystal structure. More recently the RMC method has been used for the study of crystalline materials (Mellergård & McGreevy, 1999, 2000; Tucker *et al*., 2001c). In principle, the use of the RMC method for crystalline materials could be carried out in exactly the same way as for liquids and amorphous materials. The main difference between the two types of data is that there are sharp Bragg peaks in the crystalline case that are absent in data from liquids and amorphous materials. However, in the basic methodology of RMC this difference is not significant. Sharp Bragg peaks imply structural order over effectively infinite distances. On the other hand, the

RMC configuration is of finite size of the order of 1000 unit cells, and the $G(r)$ function can only be calculated up to the distances of size $L/2$, where L is the length of the shortest side of the RMC configuration. The Fourier transform will therefore contain truncation ripples. In order to make a valid comparison between the $i(Q)$ from an RMC configuration with experimental data, the $i(Q)$ must first be convoluted with the Fourier transform of a box function of size $L/2$:

$$i'(Q) = \frac{1}{\pi}\int_{-\infty}^{\infty} i(Q')\,\frac{\sin\left(L/2(Q-Q')\right)}{Q-Q'}\mathrm{d}Q' \qquad (16).$$

Thus the sharp Bragg peaks of the data are artificially broadened before comparing with the calculated $i(Q)$. This implies some degradation of data used in the RMC method, and, particularly for studies of crystalline materials, it would be helpful to avoid this situation.

Mellergård & McGreevy (1999, 2000) have developed a new version of the RMC program (called RMCPOW) in which the calculated $i(Q)$ is calculated for a three-dimensional grid of scattering vectors $\mathbf{Q}$, and then mapped onto the one-dimensional representation of the powder measurement. The values of $\mathbf{Q}$ that can be used are determined by the dimensions of the RMC sample. The individual calculations are broadened before being added, so that the resultant $i(Q)$ is a continuous function and not a discreet set of spikes. In principle, this broadening can be related to the experimental resolution. The main problem with this approach is that it becomes computationally demanding when measurements of Q are taken to ideally large values, because the size of the grid scales with the cube power of the maximum value of Q.

We have used a different approach, in which we combine the data for $i(Q)$ and $G(r)$ with data for the explicit intensities of the Bragg peaks. Initially we used the Pawley (1981) method to extract the intensities of Bragg peaks from the diffraction data (Tucker *et al*., 2001c). The Bragg peak intensities are incorporated into the basic RMC method by adding the following term:

$$\chi^2_{\mathrm{Bragg}} = \sum_{h,k,\ell}\left(I_{\mathrm{calc}}(hk\ell) - I_{\mathrm{exp}}(hk\ell)\right)^2/\sigma^2_{hk\ell} \qquad (17).$$

The program is called RMCBragg, and has been used for studies of quartz and cristobalite. It has been described in Tucker *et al*. (2001c).

More recently we have incorporated a full profile fitting of the diffraction data, as in Rietveld refinement, using the full resolution function for the Bragg peaks (Tucker *et al*., submitted). Thus we write down the equation for the diffraction pattern as

$$I_{\mathrm{profile}}\,(t_j) = B(t_j) + \sum_j \sum_{h,k,\ell} R(t_j - t_{hk\ell}) I_{\mathrm{Bragg}}(hk\ell) \qquad (18),$$

where $B(t_j)$ is the background at t_j, $R(t_j - t_{hk\ell})$ is the resolution function associated with an $hk\ell$ reflection, and $I_{\mathrm{Bragg}}(hk\ell)$ is the integrated intensity of the $hk\ell$ reflection, which we can write as

$$I_{\mathrm{Bragg}}(hk\ell) = L(Q_{hk\ell})\,|\,F(hk\ell)\,|^2 \qquad (19).$$

$L(Q_{hk\ell})$ is the Lorentz factor, and $|F(hk\ell)|^2$ is the square of the structure factor of the $hk\ell$ reflection. Multiplicity is accounted for by explicit calculations for all combinations

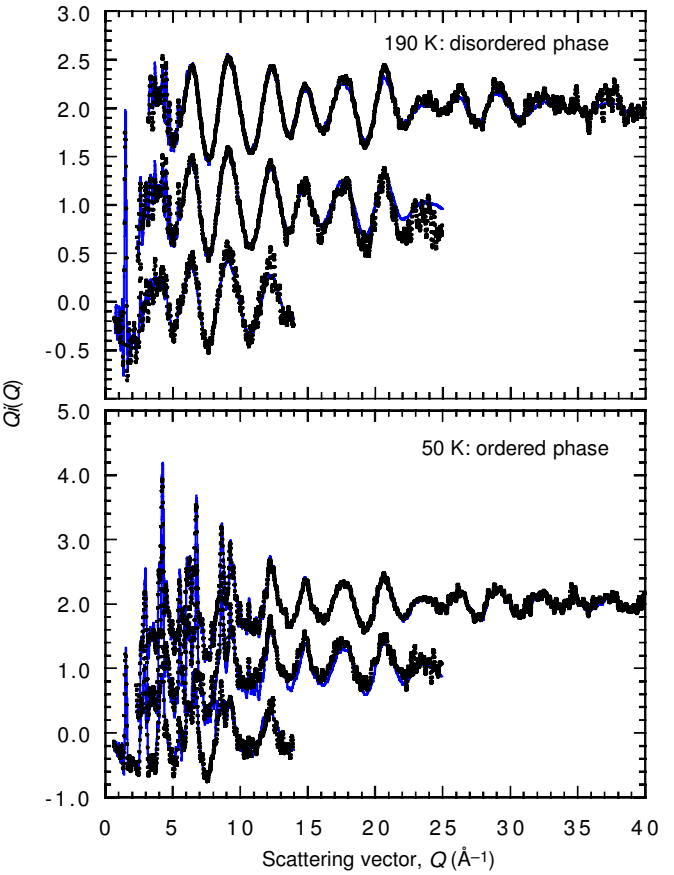

Fig. 9. $Qi(Q)$ functions for the two phases of SF_6, measured using three different banks of detectors (data points), and compared with the RMC calculations taking account of instrument resolution (continuous curves).

of $hk\ell$. The elastic scattering profile is incorporated into the RMC model through the new residual,

$$\chi^2_{\mathrm{profile}} = \sum_k \sum_j \left(I^{\mathrm{calc}}_{\mathrm{profile}}(t_j)_k - I^{\mathrm{exp}}_{\mathrm{profile}}(t_j)_k\right)^2/\sigma^2_k(t_j) \qquad (20),$$

where the sum over k denotes the inclusion of diffraction patterns from different banks of detectors (each with a different range of Q and different resolution). The background function, $B(t)$, in equation (18) arises from the diffuse scattering, and it is treated as a fitted function because it is not directly given by the computed $G(r)$. The program for this work is called RMCprofile, and will be described in detail elsewhere (Tucker *et al*., submitted).

Inclusion of the Bragg peak intensities has the merit of ensuring that the RMC method is giving both single-atom and pair distribution functions that are consistent with the full range of data, or equivalently giving both the long-range and short-range order implied by the data. RMC is clearly based in statistical mechanics, and like nature will lead to a maximisation of the entropy consistent with fulfilling the constraints of the energy function defined by χ^2. This means that the configurations produced by the RMC method will have the maximum amount of disorder possible whilst being consistent with the experimental data. What is not known is

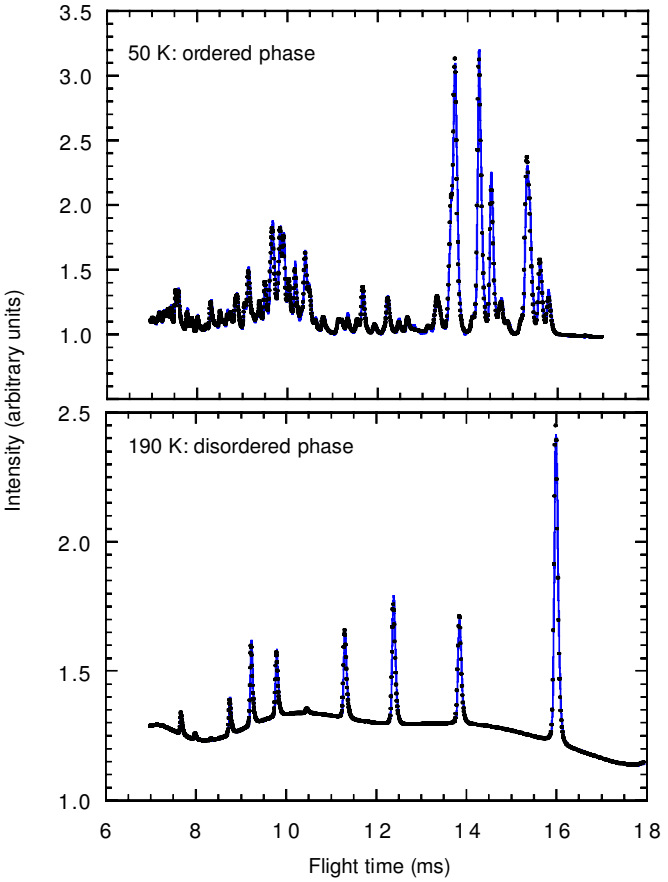

Fig. 10. Bragg diffraction profiles for the two phases of SF_6 obtained on one bank of detectors (points), and compared with the RMC calculations taking account of instrument resolution (continuous curves).

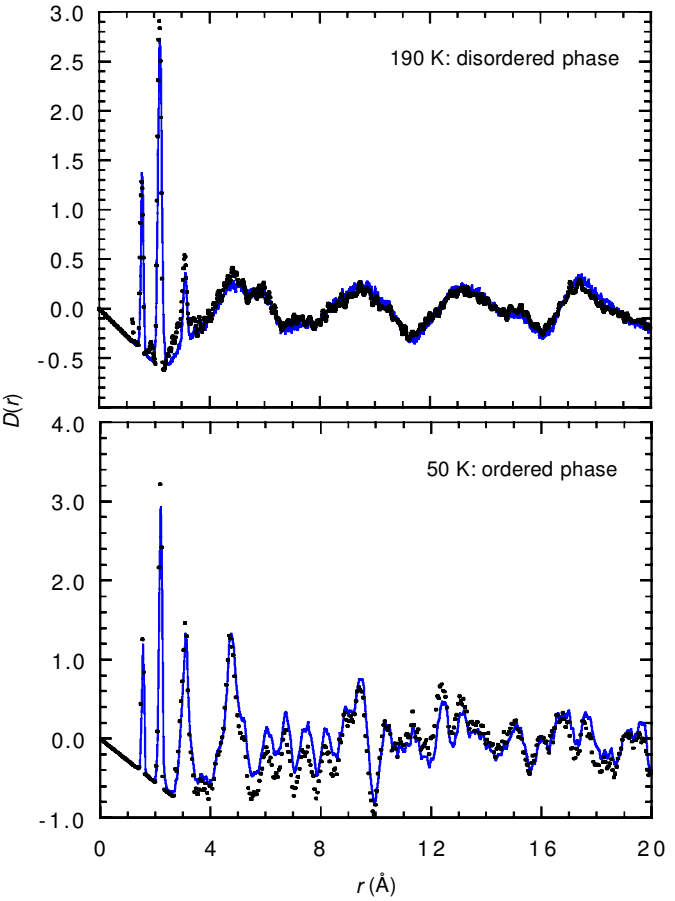

Fig. 11. Pair distribution functions $D(r)$ for the two phases of SF_6 as obtained using the MCGRtof program (points), and compared with the RMC calculations.

whether there is a wide range of configurations with equal data consistency, but with varying degrees of disorder. This is, in fact, one of the criticisms levelled at the RMC method, and is known as the uniqueness problem. We believe that this problem is rather over-stated – we would expect there to be many configurations that are consistent with the data because nature in an experiment produces many configurations that contribute to the same data set. By using as wide a set of data as possible, together with data-based constraints, the variation between different configurations of factors such as degree of order can be minimised. We have shown in Tucker *et al*. (2001c) that using different subset combinations of the data lead to very similar final configurations as measured by the χ^2 functions.

The other main advantage in using Bragg peaks is that they give to the simulation some of the three-dimensional nature of the problem. The total scattering data are strictly one-dimensional, *i.e*., the measurements are only dependent on $Q = |\mathbf{Q}|$ rather than on the truly three-dimensional $\mathbf{Q}$. It is also true that the Bragg peaks are measured in a one-dimensional sense. However, if it is possible to extract reliable values for the intensities of the Bragg peaks in the diffraction profile, the fact that each Bragg peak can be associated with a three-dimensional $\mathbf{Q} = h\mathbf{a}^* + k\mathbf{b}^* + \ell\mathbf{c}^*$ means that we do recover some of the three-dimensional nature of the problem in the data. The outcome is that we would expect the three-dimensional distribution of atom positions to be reproduced reasonably well in the RMC simulation.

Example studies

1. Example of RMC data fitting: sulphur hexafluoride

Although not a mineralogical example, recent work on the molecular crystal SF_6 highlights several of the aspects of the analysis described in this paper. There are two crystalline phases. Between 90–230 K the crystal structure is body-centred cubic, with one molecular per lattice point (Dolling *et al*., 1979). The S–F bonds lie along the $\langle 100 \rangle$ directions, but with considerable orientational disorder. This disorder has been studied in detail using molecular dynamics simulation techniques (Dove & Pawley, 1983, 1984). The origin of the orientational disorder seems to arise from the fact that when the molecules are ideally aligned in their average positions, the shortest distance between the closest F atoms of neighbouring molecules, with the interatomic vector lying along the unit cell edge, would be too short. As a result, the

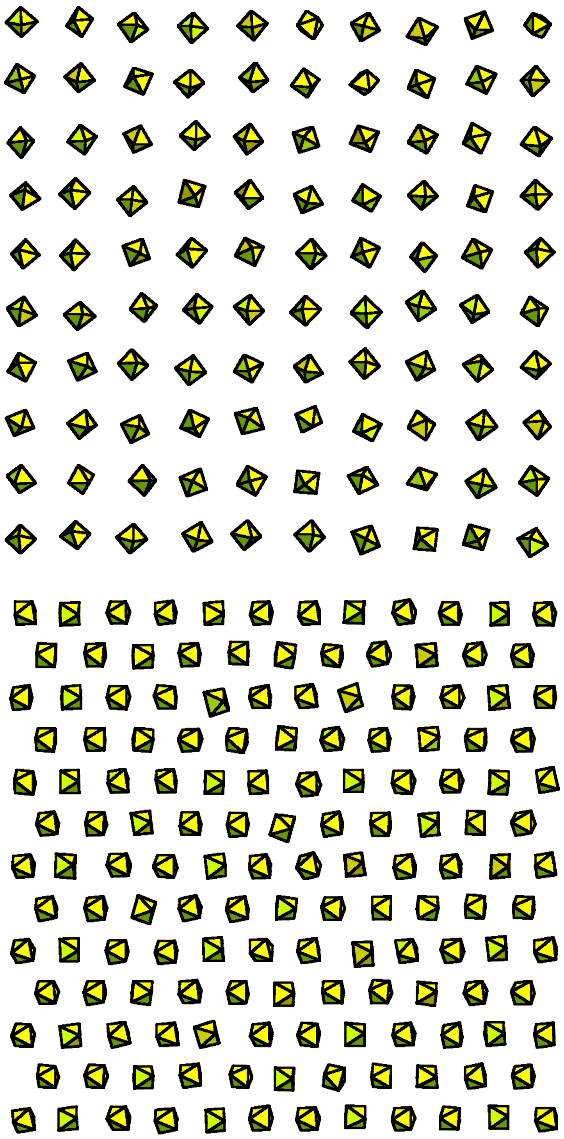

Fig. 12. RMC configurations for the disordered (top) and ordered (below) phases of SF_6. These show considerable orientational disorder of the molecules in the high-temperature phase, and ordered orientations in the low-temperature phase.

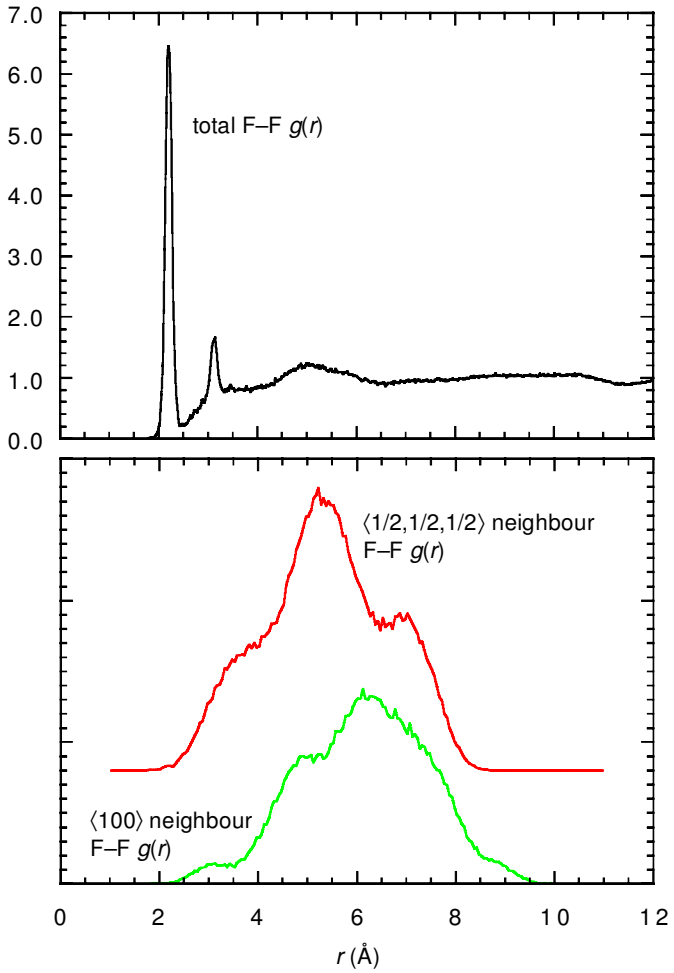

Fig. 13. *Top*, F…F distribution function of the disordered phase of SF_6 obtained from the RMC simulation and containing both inter-molecular and intra-molecular distances. *Bottom*, Corresponding inter-molecular F…F distribution function for ⟨1/2,1/2,1/2⟩ and ⟨100⟩ neighbouring molecules.

molecules are constantly pushing each other out of the way, and this results in tumbling motions of the molecules. This problem is resolved at low temperatures by a phase transition to an ordered structure with monoclinic symmetry (Powell *et al*., 1987; Dove *et al*., 1988).

Figure 9 shows the set of $Qi(Q)$ data from different banks of detectors on GEM for both phases of SF_6, which have been fitted by the MCGRtof program. Figure 10 shows the normal diffraction pattern, $I(t)$, for both phases fitted by the profile fitting part of RMCprofile. The $D(r)$ functions are shown in Fig. 11. Examples of layers of molecules from the resultant RMC configurations of both phases are shown in Fig. 12.

The intermolecular F…F pair distribution functions for the disordered phase highlight how it is possible to extract information from the RMC simulations. The main interest concerns the shortest F…F contacts along along ⟨100⟩. Given the S–F distance of 1.565 Å obtained from the total $T(r)$, and the unit cell parameter of 5.89 Å, the shortest F…F distance to be 2.76 Å if the molecules were in ordered orientations. However, it was argued on the basis of molecular dynamics simulations (Dove & Pawley 1983, 1984) that this contact distance would lead to too close an overlap of the electron distribution in the two atoms, and that the molecules would reorient in a disordered manner in order to allow the shortest contact distances to expand. This process should be seen in the F…F distribution functions. Unfortunately, these are complicated functions, because for two molecules there will be 36 distances. In Fig. 13 we show the $g(r)$ function for all F…F contacts, including both inter-molecular and intra-molecular. It is not possible to draw any conclusions from this function. In Fig. 13 we also show the components for two distinct sets of inter-molecular contacts. The most important component is that for neighbouring molecules along ⟨100⟩. The small peak at the

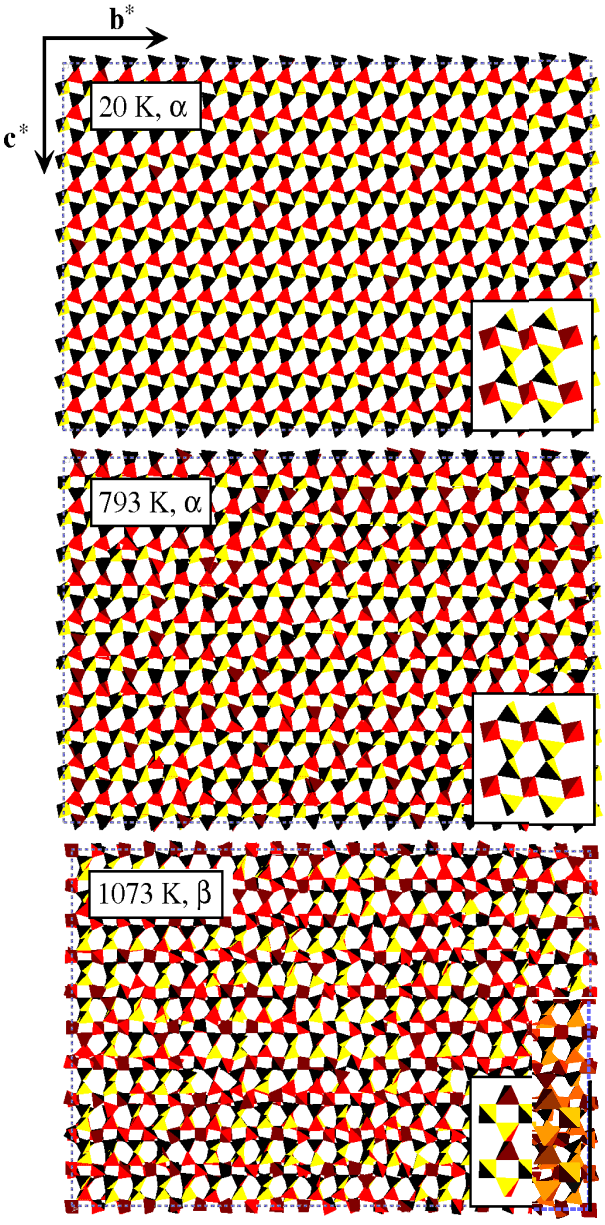

Fig. 14. (100) layers from RMC atomic configurations of quartz for two temperatures in the α-phase and one in the β-phase. SiO_4 units are represented by tetrahedra. The insets show the average structures obtained from the same configurations. In this projection the small parallelopiped spaces between tetrahedra become rectangles in the β-phase, giving a clear representation of the symmetry change associated with the phase transition (from Tucker *et al*., 2000a, 2001b)

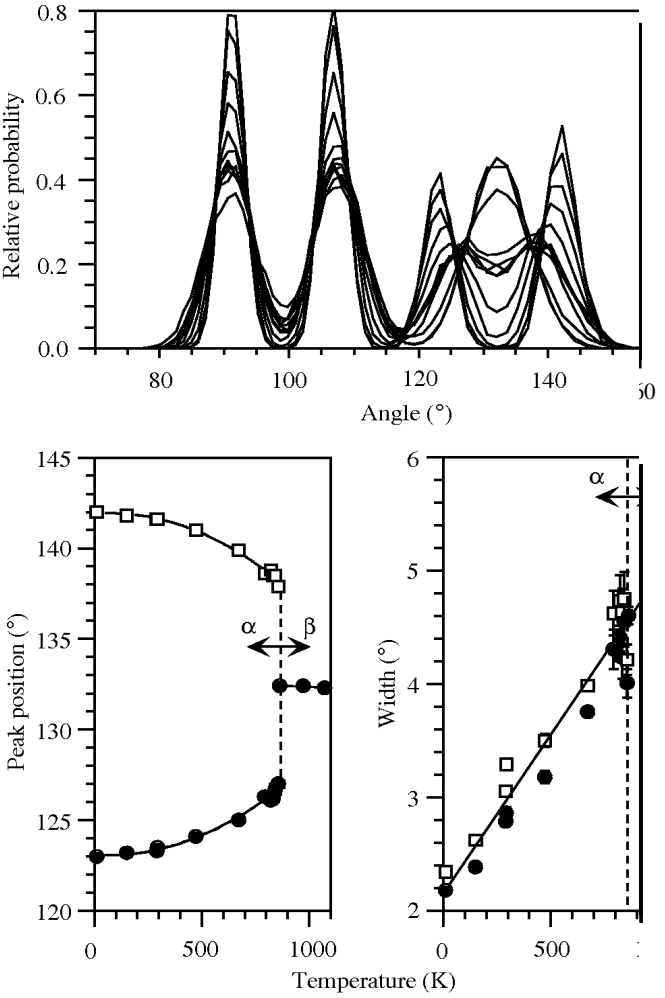

Fig. 15. *Top*, Si–Si–Si angle distribution function of quartz obtained by analysis of the RMC configurations for all temperatures indicated in Fig. 6. The lower temperatures give the sharper peaks. Note that on heating the two peaks in the range 120–150° merge to give a single peak at 132.5°. *Bottom left* shows the temperature dependence of the midpoints of the two peaks that merge, and *bottom right* shows the temperature dependence of the widths of the peaks that merge. The positions of the peaks clearly show a dependence on the α–β phase transition, whereas the widths of the peaks are virtually insensitive to the phase transition (from Tucker *et al*., 2000a).

low-*r* side of the distribution function is that corresponding to the shortest contact along ⟨100⟩. It can be seen that the position of the peak is increased from the value of 2.76 Å cited above to a value of 3 Å. This is consistent with the values expected from the molecular dynamics simulation analysis (Dove & Pawley, 1983, 1984). The important point illustrated by this analysis, however, is that it is possible to obtain detailed information about specific aspects of the sample, information that may otherwise be hidden in overall distribution functions.

2. Changes in structure arising from phase transitions in quartz and cristobalite

The RMC study of quartz (Tucker *et al*., 2000a, 2001b) is interesting as giving an illustration of the changes in both short-range and long-range order that can accompany a displacive phase transition. The $D(r)$ data for quartz shown in Fig. 6 highlight several aspects of the change in structure through the displacive phase transition. It can be seen that the lower-*r* peaks have very little temperature dependence. The variation of the instantaneous Si–O bond length shown

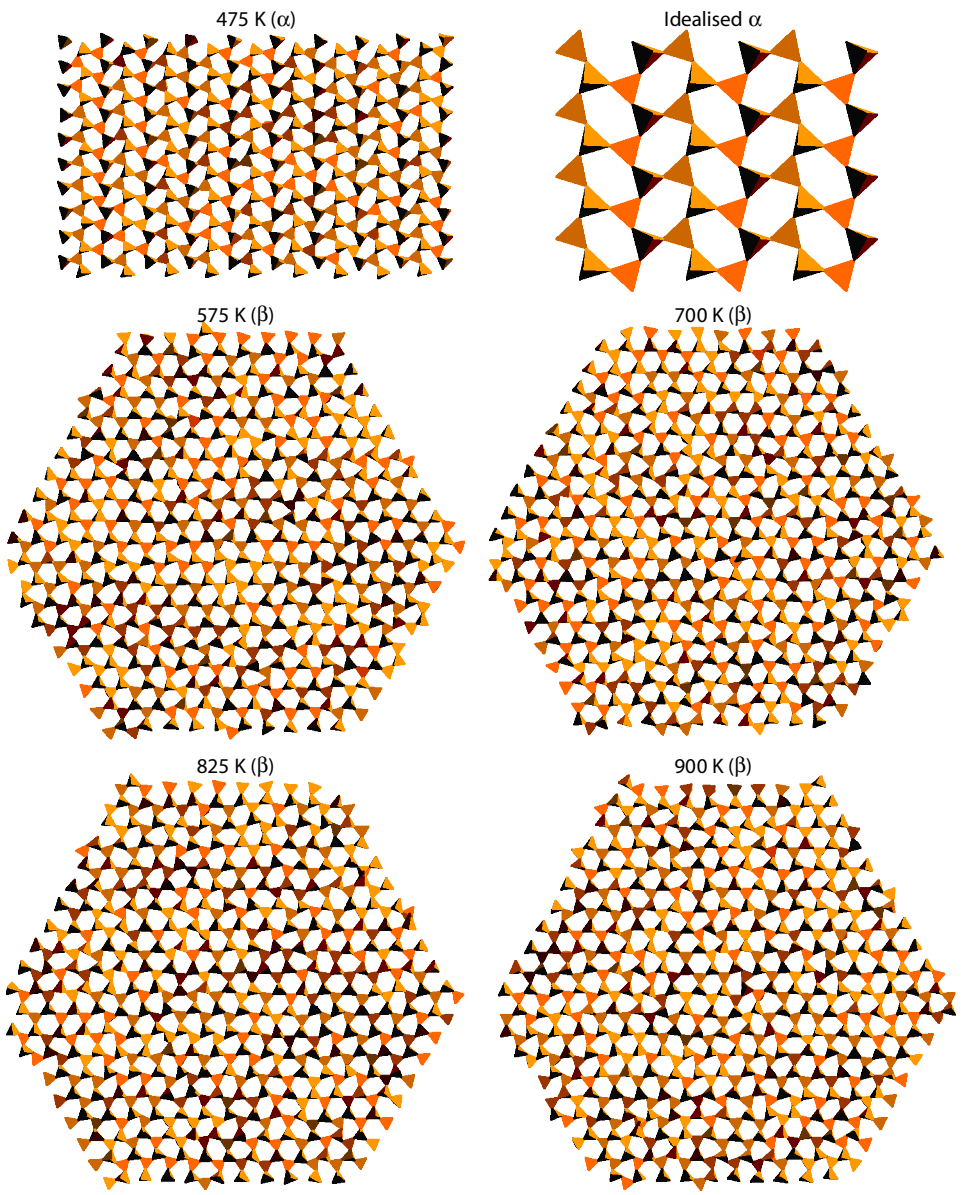

Fig. 16. Polyhedral representations of the RMC configurations of the high and low temperature phases of cristobalite, viewed down a common direction that corresponds to [1,1,1] in β-cristobalite (Tucker *et al.*, 2001a).

in Fig. 7 shows no clear change at the transition temperature, unlike the distance between the mean Si and O positions. The same is also true for cristobalite (data shown in Fig. 8). On the other hand, the positions of some of the peaks at higher values of r in the quartz $D(r)$ data of Fig. 6 do show a temperature dependence that reflects the temperature dependence of the crystal volume, which is itself strongly affected by the phase transition. Thus we see that data for different length scales are affected by the phase transition in different ways. The other important point to note is that with increasing temperature the features in $D(r)$ for quartz are broadened on heating, showing the effects of thermal disorder.

(110) layers of atomic configurations from the RMC simulations of quartz at three temperatures are shown in Fig. 14, one for the α-phase at very low temperature, one at a temperature just below the α–β phase transition, and one in the β-phase. This particular projection was chosen because the shear of the structure can be seen relatively easily (note the inserts showing the average structure, particularly the small channel between SiO_4 tetrahedra with a rectangular projection in β-quartz that is sheared in α-quartz). There are two important points to note. *First* is that the RMC simulation has produced a very ordered structure at low temperature. This highlights that a careful RMC simulation does not necessarily give an exaggerated degree of disorder. The *second* point is that there is a considerable degree of disorder of the structure, with large-amplitude rotations of the SiO_4 tetrahedra, at high temperatures, in both the α and β phases.

The change in short-range and long-range order in quartz on heating through the phase transition can be seen in three-atom distribution functions calculated from the RMC configurations. Figure 15 shows the distribution functions for the Si–Si–Si angles. At low temperatures the distribution function has four peaks. On heating towards

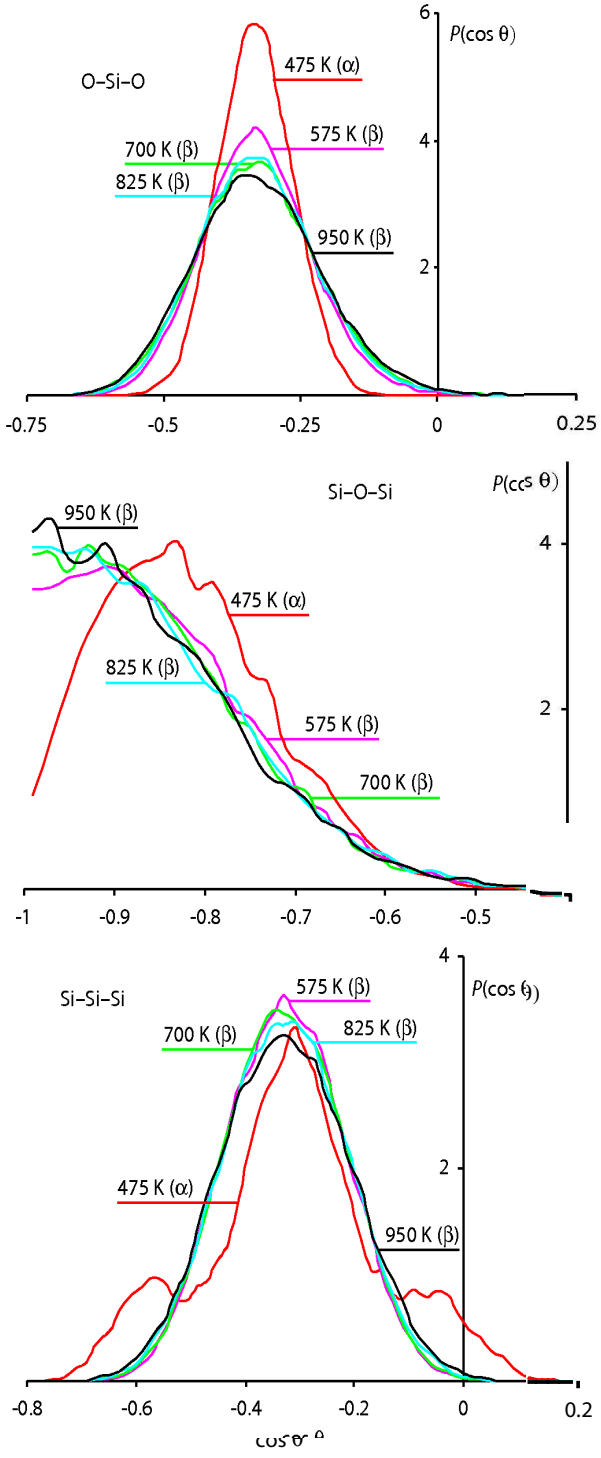

Fig. 17. Distribution functions for the O–Si–O (*top*) , Si–O–Si (*middle*) and Si–Si–Si (*bottom*) angles in the two phase of cristobalite obtained from the RMC analysis (Tucker *et al*., 2001a). Note that only the O–Si–O distribution function has any clear variation with temperature in the β-phase, but that the all the distribution functions for the α-phase are markedly different from the corresponding functions in the β-phase.

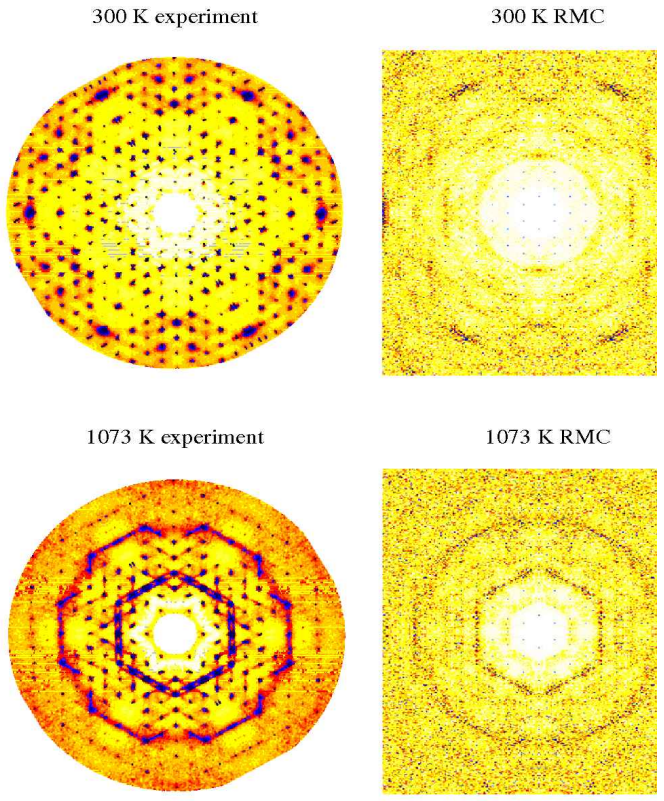

Fig. 18. Comparison of the diffuse scattering in the (*hk*0) layer reciprocal lattice of quartz measured by single-crystal neutron diffraction and calculated from the RMC configurations at a temperature in each of the two phases (Tucker *et al*., 2001b). The RMC data show the Bragg peaks as single pixels, whereas the Bragg peaks in the experimental data are broadening by experimental resolution and therefore appear as more prominent features.

the α–β phase transition, two of the peaks broaden and their midpoints become closer. In the β-phase, the two peaks merge into a broad single peak. The midpoints and widths of these peaks are shown as functions of temperature in Fig. 15. The temperature-dependence of the midpoints clearly reflects the change in long-range order associated with the phase transition. The fact that the Si–Si–Si angle distribution function clearly reflects the phase transition means that the changes in long-range order are felt down to the length scale of two neighbouring tetrahedra (the second-neighbour Si…Si distance is *ca.* 6 Å). It is sometimes argued that the structure of β-quartz consists of small domains of α-quartz, but the analysis of the Si–Si–Si angle distribution function shows that the structural changes associated with the phase transition are clearly felt at the length scale of the unit cell. On the other hand, the widths of the peaks in the Si–Si–Si angle distribution function, shown in Fig. 15, increase significantly on heating, without any change associated with the phase transition. These results shows that there are considerable fluctuations of the Si–Si–Si angle, as reflected in the configuration plots of Fig. 14. The changes in the long-range order occur on a significant background of large-amplitudes short-range disorder.

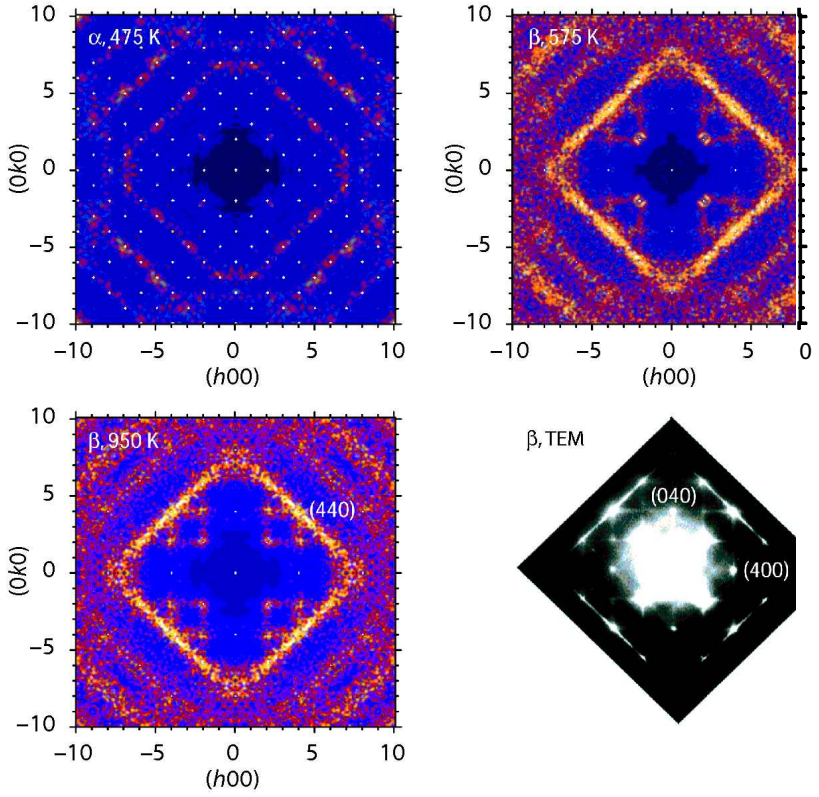

Fig. 19. Calculated [001] zone diffuse scattering for the two phases of cristobalite (including two temperatures in the high-temperature disordered phase), compared with TEM measurements (Hua *et al*., 1988) of the diffuse scattering in the high-temperature phase (Tucker *et al*., 2001a). The RMC data show the Bragg peaks as single pixels, whereas the Bragg peaks in the experimental data are broadening by experimental resolution and therefore appear as more prominent features.

Figure 16 shows layers of the RMC configurations of cristobalite in both α and β phases (Tucker *et al*., 2001a). We have shown elsewhere (Dove *et al*., 1997; Tucker *et al*., 2001a) that there is little variation in the structure of β-cristobalite with temperature. The configuration of β-cristobalite shows a considerable degree of disorder of the SiO_4 tetrahedra, and there is also a relatively high degree of disorder in the structure of α-cristobalite (albeit less than in the β-phase). The changes of structure are also shown by the Si–Si–Si angle distribution function, shown in Fig. 17. This function shows a large central peak with two side peaks in α-cristobalite, but only one peak in β-cristobalite. As for quartz, this shows that the structure of the β-phase is distinct from that of the α-phase over the length scale of one unit cell (this is also clearly seen in the O–O pair distribution functions, Tucker *et al*., 2001a), but that there is a considerable degree of short-range disorder. For completeness, we note that similar results have been obtained from an RMC analysis of the high-temperature phase of tridymite (Dove *et al*., 2000).

3. Calculations of three-dimensional diffuse scattering

An interesting challenge is to use the RMC configurations, produced by the one-dimensional total scattering and some three-dimensional Bragg peaks, to generate three-dimensional patterns of diffuse scattering. These can then be compared with single-crystal diffuse scattering experiments. Such comparisons for quartz (Tucker *et al*., 2001b) and cristobalite (Tucker *et al*., 2001a) are shown in Fig. 18 and 19 respectively. The reader should note that the Bragg scattering in the RMC maps is presented as single-pixel points, whereas the Bragg scattering in the experimental data is broadened by the instrumental resolution and hence appears more prominent than in the RMC maps. The experimental data for α- and β-quartz are from neutron scattering measurements on the PRISMA spectrometer at ISIS (Tucker *et al*., 2001b). The experimental data for β-cristobalite are from TEM measurements (Hua *et al*., 1988). The agreement between the experimental data and the RMC reconstruction is very good in each case. That may not be too surprising, since the streaks of diffuse scattering are associated with rigid unit modes, and these arise from the pattern of constraints imposed by the three-dimensional network of corner-linked SiO_4 tetrahedra. On the other hand, the encouraging point about the quality of the comparisons is that the RMC simulations have reproduced the physics of the dynamics of these systems.

In fact, it is possible to quantify the agreement between the calculated diffuse scattering and the experimental data. The calculated and measured temperature dependence of the diffuse scattering in quartz (Tucker *et al*., 2001b) are compared in Fig. 20. This is a much stricter test, because it relies on being able to calculate the intensity of the diffuse scattering and its variation through a phase transition, rather than simply calculating a pattern of diffuse scattering. It can be seen that the RMC has reproduced the experimental data in both phases. We are therefore able to conclude that the RMC method is able to properly capture the three-dimensional physics of the system under study.

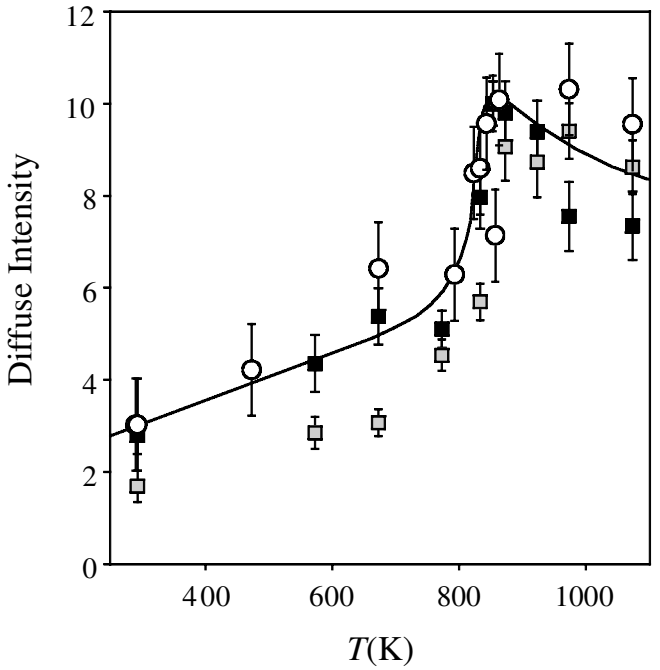

Fig. 20. Temperature dependence of the diffuse intensity from quartz in the (ζ00) directions. The circles correspond to values from the diffuse scattering obtained from RMC configurations around (4.5,3.5,0), whereas the other data points correspond to the experimental diffuse intensity at (2.5,1.5,0) and (4.5,3.5,0) (grey and black squares, respectively). The line is a guide to the eye through the circles and black squares. All plots have been scaled to give a maximum of 10 at the transition temperature (Tucker *et al.*, 2001b).

Summary

The central point of this review has been to highlight the way in which neutron total scattering measurements, by combining both Bragg diffraction and diffuse scattering in a single experiment, can provide information about long-range and short-range order simultaneously. This is particularly useful for the study of disordered crystalline materials, when the local structure fluctuates strongly from the structure averaged over all unit cells. Key examples of this are the crystalline silica phases. The Reverse Monte Carlo method facilitates the development of structural models that are consistent with the data in all aspects and across all length scales, through fitting to the total scattering intensity across a wide range of Q, to the pair distribution function, and to the intensities of the Bragg peaks. Our work in this area has mostly focussed on disordered crystalline materials, but the RMC method can also be applied to glasses (Keen, 1997), magnetic materials (Keen & McGreevy, 1991; Keen *et al.*, 1995, 1996; Karlsson *et al.*, 2000; Mellergård & McGreevy, 2000), and crystalline materials with site disorder (Mellergård & McGreevy, 2000). The RMC method has been applied to neutron single crystal diffuse scattering data (Nield *et al.*, 1995; see also Proffen & Welberry, 1997a,b, and Welberry & Proffen, 1998, for the application of the RMC method to the analysis of single-crystal X-ray diffuse scattering data), but the restricted range of Q that can be obtained in such measurements as compared to the range of Q accessible in total scattering measurements means that it is not possible to achieve the same resolution in real space.

Appendix: correction of total scattering data for background scattering and beam attenuation

A total scattering experiment requires a number of measurements in addition to that involving the sample. These are a measurement with an empty instrument, a measurement with empty sample environment equipment, and a measurement with an empty sample container within the sample environment equipment. We label the measured intensity from each of these as $I_{\rm I}$ (empty instrument), $I_{\rm E}$ (sample environment equipment), and $I_{\rm C}$ (sample container), together with $I_{\rm S}$ for the measured intensity from the sample. We denote the expected intensity, after accounting for all corrections, with a prime, as I', with the same subscripts. The relationships between the measured intensities and the expected intensities can be can be written as the following set of equations:

$$\begin{aligned} I_{\rm E} &= \alpha^{\rm E}_{\rm E} I'_{\rm E} + I'_{\rm I} \\ I_{\rm C} &= \alpha^{\rm C}_{\rm C,E} I'_{\rm C} + \alpha^{\rm E}_{\rm C,E} I'_{\rm E} + I'_{\rm I} \\ I_{\rm S} &= \alpha^{\rm S}_{\rm S,C,E} I'_{\rm S} + \alpha^{\rm C}_{\rm S,C,E} I'_{\rm C} + \alpha^{\rm E}_{\rm S,C,E} I'_{\rm E} + I'_{\rm I} \end{aligned} \qquad (21).$$

The α coefficients give the corrections for each contribution. The component in the *superscript* of each α coefficient denotes the source of scattering, and the *subscript* denotes the source of attenuation. The values of all the α coefficients can be calculated from knowledge of the components of the experiment. It is assumed that $I'_{\rm I} = I_{\rm I}$. For example, the measured intensity from the empty sample environment is given by the intensity from the empty instrument together with scattering from the sample environment that is also attenuated by the sample environment. The measured intensity of scattering from the empty container consists of the background from the instrument, a component of scattering from the sample environment equipment attenuated by both the sample container and the sample environment equipment, and a component of scattering from the sample container which is also attenuated by the sample container and the sample environment equipment.

In practice, the measurements from both the empty instrument and the instrument containing the empty sample environment, $I_{\rm I}$ and $I_{\rm E}$ respectively, can be combined to yield $I'_{\rm E}$. This is then combined with the measurements of the empty sample environment and the empty sample can within the sample environment, $I_{\rm I}$ and $I_{\rm C}$ respectively, to give $I'_{\rm C}$. Finally, all these separate components of the scattering are combined with the measurement from the sample to recover the true scattering from the sample alone, $I'_{\rm S}$. These corrections are usually applied in a single program, such as ATLAS (Hannon *et al.*, 1990), into which is read

details such as the geometry of the instrument, sample environment and sample can.

Acknowledgements: We are grateful to EPSRC for support.

References

Bacon, G.E. (1975): Neutron diffraction (third edition). Clarendon Press (Oxford). 636 p.

Billinge, S.J.L. & Thorpe, M.F. (ed) (1998): Local structure from diffraction. Plenum, New York. 412 p.

Chieux, P. (1978): Liquid structure investigation by neutron scattering. *in* "Neutron Diffraction", H. Dachs, ed. Springer-Verlag, Berlin, 271–302.

Dolling, G., Powell, B.M., Sears, V.F. (1979): Neutron diffraction study of the plastic phases of polycrystalline SF_6 and CBr_4. *Molecular Physics*, **37**, 1859–1883.

Dove, M.T. (2002): An introduction to the use of neutron scattering methods in mineral sciences. *Eur. J. Mineral.*, **14**, 000–000.

Dove, M.T. & Keen, D.A. (1999): Atomic structure of disordered materials. *in* "Microscopic properties and processes in minerals", C.R.A. Catlow, K. Wright, ed., pp 371–387.

Dove, M.T. & Pawley, G.S. (1983): A molecular dynamics simulation study of the plastic crystalline phase of sulphur hexafluoride. *J. Phys. C: Solid State Physics* **16**, 5969–5983.

—, — (1984): A molecular dynamics simulation study of the orientationally disordered phase of sulphur hexafluoride. *J. Phys. C: Solid State Physics*, **17**, 6581–6599.

Dove, M.T., Keen, D.A., Hannon, A.C., Swainson, I.P. (1997): Direct measurement of the Si–O bond length and orientational disorder in β-cristobalite. *Phys. Chem. Minerals*, **24**, 311–317.

Dove, M.T., Powell, B.M., Pawley, G.S., Bartell, L.S. (1988): Monoclinic phase of SF^6 and the orientational ordering transition. *Molecular Physics*, **65**, 353–358.

Dove, M.T., Pryde, A.K.A., Keen, D.A. (2000): Phase transitions in tridymite studied using "Rigid Unit Mode" theory, Reverse Monte Carlo methods and molecular dynamics simulations. *Min. Mag.*, **64**, 267–283.

Downs, R.T., Gibbs, G.V., Bartelmehs, K.L., Boisen, M. (1992): Variations of bond lengths and volumes of silicate tetrahedra with temperature. *Am. Mineral.*, **77**, 751–757.

Hannon, A.C., Howells, W.S., Soper, A.K. (1990): *Institute of Physics Conference Series*, **107**, 193–211.

Howe, M.A., McGreevy, R.L., Howells, W.S. (1989): The analysis of liquid structure data from time-of-flight neutron diffractometry. *J. Phys.: Cond. Matter*, **1**, 3433–51.

Hua, G.L., Welberry, T.R., Withers, R.L., Thompson, J.G. (1988): An electron-diffraction and lattice-dynamical study of the diffuse scattering in β-cristobalite, SiO_2. *J. Appl. Cryst.*, **21**, 458–465.

Karlsson, L., Wannberg, A., McGreevy, R.L., Keen, D.A. (2000): Modeling the magnetic structure of Dy_7Fe_3 metallic glass. *Phys. Rev. B*, **61**, 487–491.

Keen, D.A. (1997): Refining disordered structural models using reverse Monte Carlo methods: Application to vitreous silica. *Phase Transitions*, **61**, 109–24.

— (1998): *in* "Local Structure from Diffraction", S.J.L. Billinge and M.F. Thorpe, eds. Plenum Press, New York, 101–119.

Keen D.A. (2001): A comparison of various commonly used correlation functions for describing total scattering. *J. Appl. Cryst.*, **34**, 172–177.

Keen, D.A., Bewley, R.I., Cywinski, R., McGreevy, R.L. (1996): Spin configurations in an amorphous random-anisotropy magnet. *Phys. Rev. B*, **54**, 1036–1042.

Keen, D.A. & Dove, M.T. (1999): Comparing the local structures of amorphous and crystalline polymorphs of silica. *J. Phys.: Condensed Matter*, **11**, 9263–9273.

—, — (2000): Total scattering studies of silica polymorphs: similarities in glass and disordered crystalline local structure. *Min. Mag.*, **64**, 447–457.

Keen, D.A. & McGreevy, R.L. (1991): Determination of disordered magnetic-structures by RMC modeling of neutron-diffraction data. *J. Phys.: Condensed Matter*, **3**, 7383–7394.

Keen, D.A., McGreevy, R.L., Bewley, R.I., Cywinski, R. (1995): Magnetic-structure determination of amorphous materials using RMC modeling of neutron-diffraction data. *Nucl. Instr. Methods Phys. Research A*, **354**, 48–52.

McGreevy, R.L. & Pusztai L. (1988): Reverse Monte Carlo simulation: A new technique for the determination of disordered structures. *Molecular Simulations*, **1**, 359–67.

McGreevy, R.L. (1995): RMC – progress, problems and prospects. *Nucl. Inst. Methods Phys. Research A*, **354**, 1–16.

Mellergård, A. & McGreevy, R.L. (1999): Reverse Monte Carlo modelling of neutron powder diffraction data. *Acta Cryst. A*, **55**, 783–789.

—, — (2000): Recent developments of the RMCPOW method for structural modelling. *Chem. Phys.*, **261**, 267–274.

Nield, V.M., Keen, D.A., McGreevy, R.L. (1995): The interpretation of single-crystal diffuse-scattering using Reverse Monte Carlo modeling. *Acta Cryst. A*, **51**, 763–771.

Pawley, G.S. (1981): Unit cell refinement from powder diffraction scans *J. Appl. Cryst.*, **14**, 357–61.

Powell, B.M., Dove, M.T., Pawley, G.S., Bartell, L. (1987): Orientational ordering phase transition and the low temperature structure of SF_6. *Molecular Physics*, **62**, 1127–1141.

Proffen, T. & Welberry, T.R. (1997a): An improved method for analysing single crystal diffuse scattering using the Reverse Monte Carlo technique. *Zeit. Kristall.*, **212**, 764–767.

—, — (1997b): Analysis of diffuse scattering *via* the reverse Monte Carlo technique: A systematic investigation. *Acta Cryst. A*, **53**, 202–216.

Pusztai, L. & McGreevy, R.L. (1997): MCGR: An inverse method for deriving the pair correlation function from the structure factor. *Physica B.*, **234–6**, 357–358.

Redfern, S.A.T. (2002): Neutron powder diffraction of minerals at high pressures and temperatures: some recent technical developments and scientific applications. *Eur. J. Mineral.*, **14**, 251–261.

Schmahl, W.W., Swainson, I.P., Dove, M.T., Graeme-Barber, A. (1992): Landau free energy and order parameter behaviour of the α–β phase transition in cristobalite. *Zeit. Kristall.*, **201**, 125–145.

Tucker, M.G., Dove, M.T., Keen, D.A. (2000a): Simultaneous analyses of changes in long-range and short-range structural order at the displacive phase transition in quartz. *J. Phys.: Condensed Matter*, **12**, L723–L730.

—, —, — (2000b): Direct measurement of the thermal expansion of the Si–O bond by neutron total scattering. *J. Phys.: Condensed Matter*, **12**, L425–L430.

Tucker, M.G., Squires, M.D., Dove, M.T., Keen, D.A. (2001a): Dynamic structural disorder in cristobalite: Neutron total scattering measurement and Reverse Monte Carlo modelling. *J. Phys.: Condensed Matter*, **13**, 403–423.

Tucker, M.G., Keen, D.A., Dove, M.T. (2001b): A detailed structural characterisation of quartz on heating through the α–β phase transition. *Min. Mag.*, **65**, 489–507.

Tucker, M.G., Dove, M.T., Keen, D.A. (2001c): Application of the Reverse Monte Carlo method to crystalline materials. *J. Appl. Cryst.*, **34**, 780-782.

—, —, — (2002a): MCGRtof: Monte Carlo $G(r)$: with resolution corrections for time-of-flight neutron diffractometers. *J. Appl. Cryst.* (in press).

Welberry, T.R. & Proffen, T. (1998): Analysis of diffuse scattering from single crystals *via* the reverse Monte Carlo technique. I. Comparison with direct Monte Carlo. *J. Appl. Cryst.*, **31**, 309–317.

Williams, W.G., Ibberson, R.M., Day, P., Enderby, J.E. (1997): GEM: General materials diffractometer at ISIS. *Physica B*, **241**, 234–236.

Wright, A.C. (1993): Neutron and X-ray amorphography. *in* "Experimental techniques of glass science", ed. Simmons C.J. and El-Bayoumi (Ceramic Transactions, American Ceramic Society, Westerville), pp 205–314.

— (1994): Neutron scattering from vitreous silica. V. The structure of vitreous silica: What have we learned from 60 years of diffraction studies? *J. of Non-Crystalline Solids*, **179**, 84–115.

— (1997): X-ray and neutron diffraction, *in* "Amorphous Insulators and Semiconductors", ed. M.F. Thorpe and M.I. Mitkova, NATO ASI series 3. High Technology (Kluwer, Amsterdam), **23**, 83–131.

Received 18 July 2001
Modified version received 12 September 2001
Accepted 6 November 2001